Journal of Materials Chemistry A



PAPER

View Article Online
View Journal | View Issue



Cite this: J. Mater. Chem. A, 2024, 12, 20437

Received 7th May 2024 Accepted 5th July 2024

DOI: 10.1039/d4ta03191a

rsc.li/materials-a

Atomic doping to enhance the p-type behavior of BiFeO₃ photoelectrodes for solar H₂O₂ production†

Daye Seo,‡^a Andrew Grieder,‡^b Andjela Radmilovic,‡^a Sophya F. Alamudun,^a Xin Yuan,^a Yuan Ping **D** and Kyoung-Shin Choi **D****

BiFeO $_3$ is a semiconductor with a bandgap of \sim 2.2 eV and with conduction band minimum (CBM) and valence band maximum (VBM) positions straddling the water reduction and oxidation potentials. These features make BiFeO $_3$ a promising photoelectrode candidate for use in a photoelectrochemical cell for solar fuel and chemical production. Previous studies have shown that both n-type and p-type BiFeO $_3$ can be obtained without intentional extrinsic doping, which means that both donor- and acceptor-type defects can form readily. In this study, we prepared and compared p-type BiFeO $_3$ with intrinsic doping (acceptor levels created by Bi vacancies) and extrinsic doping (acceptor levels created by substitutional doping of Na $^+$ at the Bi $^{3+}$ site) to understand their differences using combined experimental and computational studies. We show that Na-doped BiFeO $_3$ can generate a significantly higher cathodic photocurrent density because Na doping enhances both photon absorption and electron-hole separation. Our computational results provide a microscopic understanding of their origins. We also demonstrate the use of a Na-doped BiFeO $_3$ photocathode with Ag nanoparticle catalysts for solar O $_2$ reduction to H $_2$ O $_2$ and evaluate how much photovoltage can be gained by the use of Na-doped BiFeO $_3$ photocathode.

Introduction

Bismuth iron oxide (BiFeO₃) is a semiconductor with an ABO₃-type perovskite structure in which Bi³⁺ in the A site is dodecahedrally coordinated by 12 O²⁻ and Fe³⁺ in the B site is octahedrally coordinated by 6 O²⁻.¹ Unlike the ideal perovskite, BiFeO₃ has a non-centrosymmetric structure caused by a rhombohedral distortion, and the resulting ferroelectricity has motivated the intensive investigation of BiFeO₃ for applications in electronics.²-⁴ Recently, BiFeO₃ has also been investigated as a photoelectrode for solar water splitting.⁵-¹² It has been shown to have a relatively narrow bandgap of $\sim\!2.2$ eV and conduction band minimum (CBM) and valence band maximum (VBM) positions that straddle the water reduction and oxidation potentials, 8,11,12 all of which are very favorable characteristics for a photoelectrode for use in a water-splitting or related photoelectrochemical cell.

Previous studies have shown that both n-type and p-type BiFeO₃ can be obtained without intentional doping.⁵⁻⁹ This

means that both donor- and acceptor-type defects can form readily and the dominant defect type can vary depending on the synthesis conditions.¹³ The defects that can serve as donors and induce n-type behavior include oxygen vacancies, while the defects that can serve as acceptors and induce p-type behavior include Bi vacancies.¹⁴⁻¹⁶ Since both donor- and acceptor-type defects can readily form and coexist in BiFeO₃, the concentration of the majority carrier in n-type or p-type BiFeO₃ formed without intentional doping is not considerably higher than that of the minority carrier. These lightly doped BiFeO₃ photoelectrodes are not optimal for evaluating the advantages and limitations of BiFeO₃ as a photoanode or a photocathode material.

In our recent study, we presented a new electrodeposition-based synthesis method to prepare BiFeO₃ electrodes.¹⁷ In this method, Bi and Fe metals are co-electrodeposited with a Bi: Fe ratio of 1:1 and then oxidized by thermal annealing in air to produce BiFeO₃ electrodes. The BiFeO₃ electrodes prepared by this method are n-type, meaning that under these synthesis conditions, more donor-type defects formed than acceptor-type defects. For the reason explained above, these n-type BiFeO₃ electrodes obtained without intentional doping are very lightly doped. In order to increase the free electron concentration, we additionally annealed the n-type BiFeO₃ electrodes under a N₂ environment to introduce more oxygen vacancies that can serve as donors. Using the resulting electrodes, we were able to

^aDepartment of Chemistry, University of Wisconsin-Madison, Madison, WI 53706, USA. E-mail: yping3@wisc.edu; kschoi@chem.wisc.edu

^bDepartment of Materials Science and Engineering, University of Wisconsin-Madison, Madison, WI 53706, USA

^{*}Department of Physics, University of Wisconsin-Madison, Madison, WI 53706, USA
† Electronic supplementary information (ESI) available. See DOI
https://doi.org/10.1039/d4ta03191a

[‡] These authors contributed equally to this work.

evaluate the photoelectrochemical properties of ${\rm BiFeO_3}$ photoanodes.

When it comes to p-type BiFeO₃, all reported p-type behaviors of BiFeO₃ photocathodes originated from intrinsic doping where Bi or Fe vacancies were created during synthesis either intentionally or unintentionally.^{5-7,18,19} To our best knowledge, extrinsic doping (*i.e.*, introducing an impurity atom *via* substitutional doping to create acceptor levels), which may allow the hole concentration to be increased more methodically, has not been attempted to enhance the p-type behavior of BiFeO₃.

In this study, we report combined experimental and theoretical investigations on the substitutional doping of Na⁺ at the Bi³⁺ site, which can considerably enhance p-type behavior of BiFeO₃. We prepared two different p-type BiFeO₃ electrodes, one with intrinsic doping (i.e., Bi vacancy, V_{Bi}) and the other with extrinsic doping (i.e., Na doping at the Bi site, NaBi), while keeping other factors (e.g., film thickness and morphology) comparable. By comparing photoelectrochemical properties of these photoelectrodes and relating experimental and computational results (e.g., formation energy and the ionization energy of V_{Bi} and Na_{Bi}), we elucidate the difference between intrinsic doping and extrinsic doping and offer an atomic level understanding of their effects on the photoelectrochemical properties of p-type BiFeO₃. Furthermore, using the Na-doped BiFeO₃ photocathode decorated with a Ag nanoparticle catalyst, we demonstrate solar O2 reduction to H2O2, which provides an energy-efficient and environmentally benign route for H2O2 production.20-22

Experimental

Materials

Bismuth(III) nitrate (Bi(NO₃)₃·5H₂O, 98%), sodium nitrate $(NaNO_3, 99.0\%)$, potassium perchlorate $(KClO_4, 99-100.5\%)$, dimethyl sulfoxide (DMSO, 99.9%), N,N-dimethylformamide (DMF, >99.8%), potassium iodide (KI, 99+%), potassium hydrogen phthalate (KHP, 99.95%), hydrogen peroxide (H₂O₂, 30% (w/w) in H₂O, contains stabilizer), potassium phosphate dibasic (K₂HPO₄, >98%), and potassium hydroxide (KOH, >85%) were purchased from Sigma-Aldrich. Potassium phosphate monobasic (KH₂PO₄, >99%) was purchased from Santa Cruz Biotechnology. Iron(II) chloride (FeCl₂·4H₂O, 98%) and silver(1) nitrate (AgNO3, 99.9+%) were purchased from Alfa-Aesar Chemicals. Tetrabutylammonium hexafluorophosphate (TBAPF₆, >98%) was purchased from TCI Chemicals. All chemicals were used as purchased without further purification. Glass substrates coated with fluorine-doped tin oxide (FTO) were purchased from Hartford Glass Co. and cleaned thoroughly prior to use. Nafion membrane (N211) was purchased from Fuel Cell Store.

Preparation of BiFeO₃ electrodes

To prepare pristine, stoichiometric $BiFeO_3$ electrodes, Bi and Fe were co-electrodeposited with a Bi: Fe atomic ratio of 1:1. The electrodeposition of Bi/Fe films was carried out in an undivided cell using a SP-200 (Bio-Logic Science Instrument). A typical 3-

electrode setup with an FTO working electrode, an FTO counter electrode, and a Ag/Ag⁺ (in DMSO solution containing 10 mM AgNO₃ and 0.1 M TBAPF₆) reference electrode was used. The exposed area of the FTO working electrode was \sim 1.25 cm². The plating solution was a DMSO solution containing 8 mM Bi(NO₃)₃·5H₂O, 12 mM FeCl₂·4H₂O, and 100 mM KClO₄ (supporting electrolyte). The DMSO solution was purged with Ar for 15 min before adding the metal precursors and supporting electrolyte. The resulting solution was additionally purged with Ar for 30 s to completely remove any remaining oxygen, and electrodeposition was initiated immediately after. (O2 in the solution can not only oxidize Fe2+ to Fe3+ but also be reduced during electrodeposition, affecting the reproducibility of Bi/Fe film deposition.) A constant potential of -2.1 V (vs. Ag/Ag⁺) was applied to the working electrode and the charge passed during the electrodeposition was 100 mC cm⁻². Immediately after deposition, the Bi/Fe films were soaked in ethanol and then blow-dried with air. The films were black in color and showed a uniform and compact morphology (Fig. S1†). The Bi: Fe atomic ratio of the as-deposited films determined by energy dispersive X-ray spectroscopy (EDS) was 1:1. To convert the Bi/ Fe films to BiFeO₃, the as-deposited films were annealed in air at 600 °C for 6 h (ramp rate: 1.7 °C min⁻¹). The resulting films were orange in color.

To prepare Na-doped BiFeO3 electrodes, Bi-deficient Bi/Fe films were deposited in a DMSO solution containing 8 mM Bi(NO₃)₃·5H₂O, 12.5 mM FeCl₂·4H₂O, and 100 mM KClO₄ while keeping other deposition conditions the same. The Bi: Fe atomic ratio of the as-deposited films determined by EDS was 0.93:1. A DMF solution (50 µL) containing 2 mM NaNO3 was drop-cast onto the as-deposited film, which was then annealed in air at 600 °C for 6 h (ramp rate: 1.7 °C min⁻¹). The annealed film was gently rinsed with water to remove any excess Na ions that did not incorporate into the Na-doped BiFeO3 films. The Na: Bi ratio in the Na-doped BiFeO₃ films determined by inductively coupled plasma-mass spectroscopy (ICP-MS) was 0.07: 0.93, equivalent to 7 atomic% doping of Na at the Bi site. When the Bi-deficient Bi/Fe films were thermally treated without a drop-cast solution containing Na⁺, Bi-deficient BiFeO₃ electrodes were prepared. The nominal formulae for Na-doped and Bi deficient samples are Na_{0.07}Bi_{0.93}FeO₃ and Bi_{0.93}FeO₃, respectively, assuming no phase segregation and oxygen vacancies.

Materials characterization

The surface morphology and elemental composition were determined by scanning electron microscopy (SEM; Leo Supra55 VP, accelerating voltage 2 kV) and EDS (Noran System Seven, Thermo-Fisher, ultra-dry silicon drift detector, accelerating voltage: 22 kV), respectively. The amount of Na in Nadoped BiFeO3 was analyzed by ICP-MS (ICPMS-2030, Shimadzu). The purity and crystallinity were characterized by X-ray diffraction (XRD; D8 Discover, Bruker, Ni-filtered Cu Ka radiation, $\lambda=1.5418$ Å). The band gap and light absorption property were determined from UV-visible (UV-vis) absorption spectra obtained using an integrating sphere to collect all reflected and transmitted light, allowing for more accurate determination of

absorbance (Cary 5000 UV-vis-NIR spectrophotometer, Agilent). The energy gap between the valance band minimum and Fermi level $(E_{VBM}-E_F)$ was investigated by X-ray photoelectron spectroscopy (XPS, Ka X-ray photoelectron spectrometer, Thermo Scientific) using monochromatized aluminum Ka X-ray (1486.68 eV) as the excitation source. Prior to XPS measurements, a Ag metal contact was deposited onto the BiFeO₃ electrodes using a Hummer 8.3 DC/RF Sputter System (Anatech USA) to ensure good electrical contact between the photoelectrodes and the spectrometer. The Fermi edge of the Ag metal acquired after cleaning the surface by Ar ion beam was used as a reference to calibrate the binding energies of the samples.

XRD simulations were performed using the Fullprof program package.²³ The peak shape was modeled by pseudo-Voigt function with peak parameters U = 0.05, V = -0.06 and W = 0.07. The lattice parameters, fractional coordinates of atoms, site occupations and isotropic atomic displacement parameters for pristine BiFeO3 were obtained from the ICSD database (#51664).24 The XRD pattern of Na_{0.07}Bi_{0.93}FeO₃ was simulated by replacing 7% of Bi at the Bi3+ site with Na+ while keeping other parameters constant. The XRD pattern of Na_{0.07}Bi_{0.93}FeO₃ with a (110) preferential orientation was simulated by setting the March-Dollase parameter to 0.75 in the (110) direction.

Photoelectrochemical and electrochemical characterization

All photoelectrochemical and electrochemical measurements were conducted with an SP-200 (Bio-Logic Science Instrument). Solar illumination was simulated by filtering light from a 300 W Xe arc lamp through the following successive filters: an IR filter, neutral density filters, and an AM 1.5G filter. The light was collimated and directed onto the sample via an optical fiber, and the light was calibrated to 100 mW cm⁻² (1 sun) using a National Renewable Energy Laboratory-certified GaAs reference cell (PV measurements, Inc). The illuminated area was 0.06 cm². The light was illuminated through the BiFeO₃ film side (front-side illumination). A typical 3-electrode setup was used in an undivided cell with a BiFeO3 working electrode, a Hg/HgO (1 M KOH) reference electrode, and a graphite rod counter electrode. Photoelectrochemical property of the BiFeO₃ photoelectrodes was first evaluated by obtaining photocurrentpotential (J-V) plots in 0.1 M KOH solution saturated with O₂ and with constant O₂ bubbling where O₂ was used as an electron scavenger. Chopped illumination was used so that the dark current and photocurrent densities could be measured during a single potential scan. The potential was scanned from the open circuit potential (ocp) to the negative direction with a scan rate of 10 mV s^{-1} .

All results in this work are presented with respect to the reversible hydrogen electrode (RHE) unless otherwise mentioned. Potentials vs. reference electrodes were converted to potentials vs. RHE as follows:

$$E_{(vs. RHE)} = E_{(vs. Ag/AgCl)} + E_{Ag/AgCl} + 0.0591 \text{ V} \times \text{pH}$$

or $E_{(vs. RHE)} = E_{(vs. Hg/HgO)} + E_{Hg/HgO} + 0.0591 \text{ V} \times \text{pH}$

where $E_{\rm Ag/AgCl} = 0.1976$ V vs. NHE at 25 °C and $E_{\rm Hg/HgO} = 0.1325$ V νs. NHE at 25 °C.

With the same electrolyte (O2 purged 0.1 M KOH), the wavelength-dependent photocurrent was measured, and the absorbed photon-to-current efficiency (APCE) was determined using the following equation,

IPCE(%) =
$$\frac{1240 \text{ (eV nm)} \times |J_{ph} \text{ (mA cm}^{-2})|}{P \text{ (mW cm}^{-2}) \times \lambda \text{ (nm)}} \times 100(\%)$$

APCE(%) =
$$\frac{IPCE(\%)}{1 - 10^{-A_{(\lambda)}}}$$

where IPCE is the incident photon-to-current efficiency, $J_{\rm ph}$ is the photocurrent, P is the power density of monochromatic light, λ is the wavelength, and $A_{(\lambda)}$ is the absorbance at a given wavelength.

Light source was 150 W Xe arc lamp equipped an AM 1.5G filter and neutral density filters and monochromatic light was produced by Oriel Cornerstone 130 monochromator with a 10 nm interval. The power of light at each wavelength was measured by a Si photodiode (SED 033, International Light Technologies). The photocurrent was measured while applying constant potential (0.6 V) in a home-made Faraday cage with the same potentiostat and the same 3-electrode setup mentioned above.

The maximum photocurrent that can be achieved with the photocathodes assuming that all the absorbed photons are converted to photocurrent (i.e., absorbed photon-to-current efficiency is 100%.) was calculated by the following steps. First, the National Renewable Energy Laboratory (NREL) reference solar spectral irradiance at AM 1.5G (radiation energy (W m⁻² nm⁻¹) vs. wavelength (nm))²⁵ was converted to the solar energy spectrum in terms of the number of photons (s⁻¹ m⁻² nm^{-1}) vs. wavelength (nm). Then, the number of photons at each wavelength that absorbed by the photoelectrodes was calculated by multiplying the light harvesting efficiency (1 - $10^{-A_{(\lambda)}}$). And then the total number of absorbed photons was calculated by using a trapezoidal integration (the increment of wavelength = 1 nm) and was converted to the photocurrent. The calculated maximum photocurrents of the photocathodes based on their absorbances were 5.95 mA cm⁻² and 7.06 mA cm⁻² for Bi-deficient and Na-doped BiFeO₃ electrodes respectively.

Photoelectrochemical O₂ reduction and H₂O₂ quantification

For photoelectrochemical deposition of Ag particles and H₂O₂ production, simulated solar light was generated using an LCS-100 solar simulator (Oriel Instruments) equipped with a 100 W Xe arc lamp (Newport) and an AM 1.5G filter. An infrared filter (Newport) and a focusing lens were placed between the light source and the electrode, and the intensity of light was calibrated to 1 sun (100 mW cm⁻²) at the back side of the BiFeO₃ electrode using the GaAs reference cell. The entire area of the BiFeO₃ electrodes (~1.25 cm²) was illuminated by the solar simulator. The photoelectrodeposition of Ag particles

on Na-doped BiFeO $_3$ was performed in a DMSO solution containing 2 mM AgNO $_3$ and 0.1 M TBAPF $_6$ using a Na-doped BiFeO $_3$ electrode as the working electrode. The same counter electrode and reference electrode used for electrodeposition of Bi/Fe films were used. For the photoelectrochemical deposition of Ag, a constant potential of 0.1 ν s. the Ag/Ag $^+$ reference electrode was applied (which is equivalent to making the WE potential more negative than the ocp under illumination by 0.3 V) for 1 min under continuous illumination. The resulting Agdeposited Na-doped BiFeO $_3$ electrodes were rinsed with ethanol and dried with a gentle stream of air.

For photoelectrochemical $\rm O_2$ reduction, a home-made two compartment acrylic cell was used, where the cathodic chamber and the anodic chamber were divided by a Nafion membrane. Both chambers were filled with 8 mL of 0.1 M potassium phosphate buffer (pH 7). The working electrode (Ag-deposited Na-doped BiFeO₃) and the reference electrode (Ag/AgCl in 4 M KCl) were immersed in the cathodic chamber while the counter electrode (graphite rod) was immersed in the anodic chamber. The photoelectrode was illuminated through the glass side first (back-illumination). During the photoelectrochemical cell operation, the cathodic chamber was purged with $\rm O_2$ (flow rate: 10 ccm) and gently stirred with a stirring bar. An 1 h-electrolysis was performed at the constant potential of 0.8 V νs . RHE and the amount of $\rm H_2O_2$ was quantified using iodometric titration.

For iodometric titration, 1 mL of the electrolyte used in the photoelectrochemical O₂ reduction was taken and diluted with 1 mL of DI water. Then, 1 mL of 0.25 M KHP solution and 1 mL of 0.4 M KI solution were additionally added. In this solution, photoelectrochemically generated H₂O₂ reacts with I⁻ forming I³ which absorbs light of which wavelength is 250-500 nm. KHP serves as an additional pH buffer. Absorbance at 355 nm measured by a spectrophotometer (Cary 5000 UV-vis-NIR spectrophotometer, Agilent) was used for the construction of the calibration curve and the quantification of the amount of produced H₂O₂.18 Faradaic efficiency (FE) for H₂O₂ production was calculated by dividing the charges used to produce the detected amount of H₂O₂ by the total charge passed during the electrolysis using the following equation, where n is the number of electrons required to produce one H₂O₂ molecule, which is 2, and F is Faraday's constant (96 485.33 C mol⁻¹).

$$FE(\%) = \frac{n \times \text{amount of } H_2O_2 \text{ (mol)} \times F \text{ (C mol}^{-1})}{\text{total charge passed (C)}} \times 100(\%)$$

Computational methods

Density functional theory calculations were performed using the Quantum ESPRESSO package, 26 with PBE + U exchange correlation functional, GBRV 27 pseudopotentials, and a wavefunction energy cutoff of 40 Ry and charge density cutoff of 240 Ry. The Hubbard U parameters of 2 eV on O 2p and 3 eV on Fe 3d were used. All calculations were performed with a 2 × 2 × 1 supercell of BiFeO $_3$ consisting of 120 atoms. For charged-defect calculations we applied a charge correction scheme as

discussed in previous studies. 28,29 Geometry relaxations were converged with forces on ions less than 10^{-3} Ry bohr $^{-1}$ using a 2 \times 2 \times 2 k-point grid. After relaxation a 4 \times 4 \times 4 k-point grid was used to calculate density of states. The calculation results obtained with PBE + U were compared with the results obtained by calculations with the hybrid functional HSE06. Hybrid functional calculations were performed with the Vienna *ab initio* Simulation Package (VASP) at the gamma point using plane-wave cutoff of 600 eV. The ionic positions were relaxed until the forces on all ions were less than 0.01 eV Å $^{-1}$. The results obtained from the hybrid functional HSE06 confirmed the reliability of results obtained from PBE + U as discussed below and in ESI. †

Theoretical absorption spectra were calculated using the YAMBO³² code using the single-particle eigenvalues and wavefunctions from Quantum ESPRESSO²⁶ with the same exchange correlation functional as band structure calculations above. The dielectric function was computed in the random phase approximations with local field effects. From the dielectric function the absorption spectrum (α) is computed from the real (ε_1) and imaginary (ε_2) parts of the dielectric function using eqn (1), where ω is the photon energy and c is the speed of light.

$$\alpha = \frac{\omega}{c} \frac{\varepsilon_2(\omega)}{\sqrt{\frac{\varepsilon_1(\omega) + \sqrt{\varepsilon_1(\omega)^2 + \varepsilon_2(\omega)^2}}{2}}}$$
(1)

Defect formation energies were calculated from eqn (2):

$$FE_{q}[\varepsilon_{F}] = E_{q} - E_{pst} + \sum_{i} \mu_{i} \Delta N_{i} + q \varepsilon_{F} + \Delta_{q}$$
 (2)

Here the FE $_q$ is the formation energy of a defect at charge q, E_q is the total energy of defective system, $E_{\rm pst}$ is the total energy of the pristine system, μ_i is the chemical potential of atomic species i, ΔN_i is the change in the number of atomic species i, $\varepsilon_{\rm F}$ is the Fermi energy, and Δ_q is the defect charge correction. All components of eqn (2) were computed using DFT. To avoid the formation of secondary phases the chemical potentials were determined using the following inequalities:

$$\mu_{\rm Fe} + \mu_{\rm Bi} + 3\mu_{\rm O} = E_{\rm BiFeO_3} \tag{3}$$

$$2\mu_{\rm Bi} + 3\mu_{\rm O} \le E_{\rm Bi,O_3}$$
 (4)

$$2\mu_{\rm Fe} + 3\mu_{\rm O} \le E_{\rm Fe,O},\tag{5}$$

$$2\mu_{\mathcal{O}} \le E_{\mathcal{O}_2} \tag{6}$$

$$\mu_{\text{Na}} + 2\mu_{\text{O}} \le E_{\text{NaO}_2} \tag{7}$$

The oxygen chemical potential was computed for 1 atm at 873.15 K, to match experimental annealing conditions.³³ After computing the formation energy at different charge states, we computed the charge transition levels $\varepsilon^{q|q'}$, which is the Fermi level $(\varepsilon_{\rm F})$ when the system undergoes a transition from one stable charge state q to another q' using eqn (8):

$$\varepsilon^{q/q'} = \frac{E_q^f[\varepsilon_F] - E_{q'}^f[\varepsilon_F]}{q' - q} \tag{8}$$

Results and discussion

Synthesis and characterization

The pristine, stoichiometric BiFeO₃ electrodes investigated in this study were prepared by co-electrodepositing Bi and Fe metals with a Bi: Fe atomic ratio of 1:1 (Fig. S1†), followed by annealing in air to form the desired ternary oxide phase (Fig. 1a).17 The Na-doped BiFeO3 electrodes were prepared by first electrodepositing a Bi-deficient Bi/Fe film with the Bi:Fe atomic ratio of 0.93:1. This film was annealed with a drop-cast DMF solution containing 2 mM NaNO₃ to form Na_{0.07}Bi_{0.93}FeO₃ during annealing in air. Any excess Na not incorporated into the BiFeO₃ lattice was removed by rinsing the Na_{0.07}Bi_{0.93}FeO₃ electrode with DI water (Fig. 1b). Thermal annealing without the drop-cast solution containing Na+ resulted in Bi-deficient BiFeO₃ with the nominal composition of Bi_{0.93}FeO₃ (Fig. 1c). The further decrease in the Bi: Fe ratio did not improve the ptype behavior of the resulting electrodes, suggesting that the amount of VBi and NaBi that can be stabilized in BiFeO3 are limited under our synthesis conditions.

The SEM images and photographs of pristine, Bi-deficient, and Na-doped BiFeO3 electrodes are shown in Fig. 2a-c. All electrodes showed a compact morphology, with nanosized grains. While pristine BiFeO₃ and Bi-deficient BiFeO₃ show very similar absorption spectra with their bandgap estimated to be around 2.1 eV, Na-doped BiFeO3 shows a slight redshift of the bandgap and generally enhanced absorption above the bandgap (Fig. 2d). The microscopic origin for this change caused by Na doping is explained in the computational study section.

The XRD patterns of BiFeO₃ electrodes are compared in Fig. 3a. There are no noticeable differences in XRD patterns between the pristine and Bi-deficient BiFeO3 samples in terms of the peak position, and they match well with the simulated XRD patterns of BiFeO₃ and Bi_{0.93}FeO₃ with no preferential orientation (Fig. S2a and b†). The Na-doped sample also shows no shifts in XRD patterns compared to the pristine sample. This

is expected as the ionic radii of Bi³⁺ and Na⁺ ions coordinated by the same number of O²⁻ ions are very similar.³⁴ The only noticeable difference in the XRD pattern associated with Na doping is an enhanced intensity for the (110) peak appearing at 32.1° (Fig. 3b). Using simulated XRD patterns (Fig. S2c†), we found that 7% substitutional doping of Na⁺ at the Bi³⁺ site should not enhance the intensity of the (110) peak. Thus, we suspect that the enhanced (110) peak of Na-doped BiFeO₃ is not caused by the compositional change of the films but rather the synthesis condition used for Na doping (i.e., annealing with a drop-cast DMF solution containing NaNO₃) affecting crystal growth and changing crystal orientation relative to the substrate during annealing (i.e., more crystals are oriented such that (110) planes are parallel to the substrate). Indeed, the experimental XRD pattern of the Na-doped BiFeO₃ matches well with the simulated XRD pattern of Na_{0.07}Bi_{0.93}FeO₃ with a slight (110) preferential orientation (Fig. S2d†).

We note that Bi-deficient BiFeO₃ and Na-doped BiFeO₃ show tiny impurity peaks at 42.8° and at 35.6°, respectively. The impurity phases cannot be conclusively identified with only one small broad peak appearing in each XRD pattern. However, judging from the Bi: Fe ratio being smaller than 1:1 in these samples, these impurity phases should be Fe-based oxides, which are typically n-type. Thus, we expect that the ptype properties of Bi-deficient BiFeO₃ and Na-doped BiFeO₃ would not be affected by these negligible amounts of impurities.

Photoelectrochemical properties

The effects of intrinsic and extrinsic doping on the p-type photoelectrochemical properties of the BiFeO3 electrode were evaluated using photoelectrochemical O2 reduction. O2 has been used as an electron acceptor for testing various oxide photocathodes containing Fe and Bi (e.g., LaFeO₃ and CuBi₂O₄) because their surfaces are generally much more catalytic for O2 reduction than water reduction.35,36 In fact, BiFeO3 is well known to be a good electrocatalyst for O2 reduction in basic solutions.37 Therefore, photoelectrochemical O2 reduction in basic solutions can be a good preliminarily test for assessing the

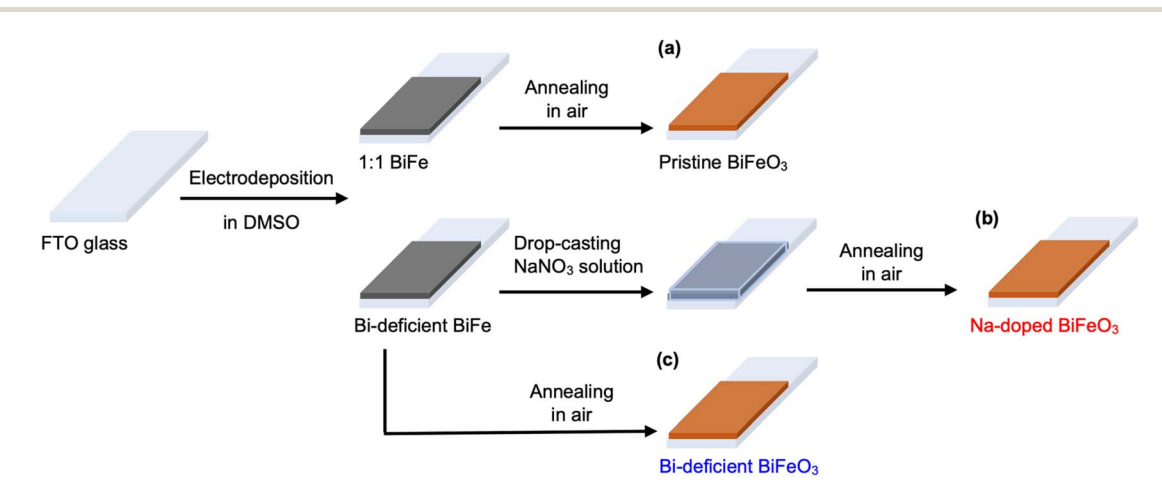


Fig. 1 Schematic representation of the synthesis procedure for (a) pristine, (b) Na-doped, and (c) Bi-deficient BiFeO₃ electrodes.



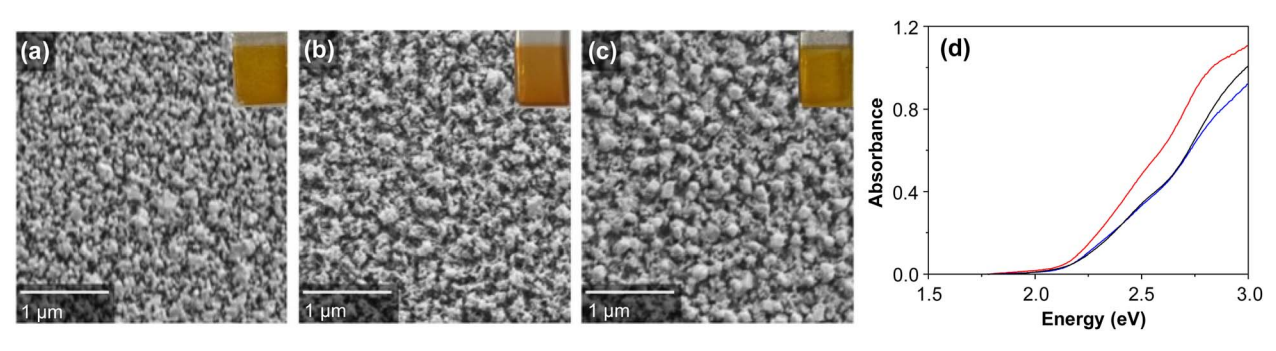


Fig. 2 SEM images of (a) pristine, (b) Bi-deficient, and (c) Na-doped BiFeO₃ electrodes. The insets show photographs of the corresponding films. (d) UV-vis absorbance comparison of pristine (black), Bi-deficient (blue) and Na-doped (red) BiFeO₃.

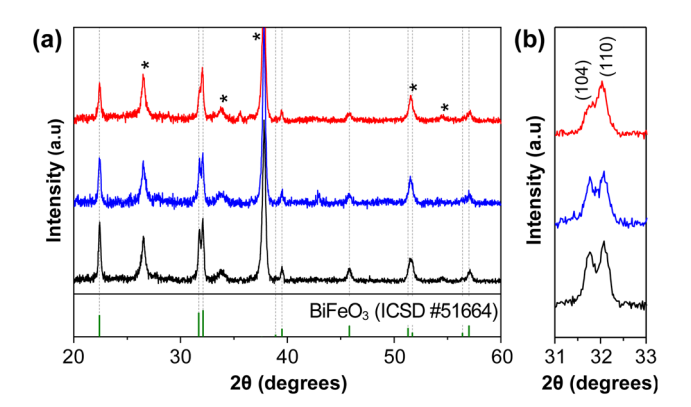


Fig. 3 (a) XRD patterns of pristine (black), Bi-deficient (blue) and Nadoped (red) $BiFeO_3$ electrodes. Peaks from the FTO substrate are marked with asterisks (*). (b) A magnified two theta region from (a) showing (104) and (110) peaks.

p-type behavior of BiFeO₃ photocathodes without needing to deposit catalysts to promote interfacial electron transfer.

Fig. 4a shows the J–V plots of Bi-deficient and Na-doped BiFeO $_3$ photocathodes acquired in O $_2$ purged 0.1 M KOH solution under AM 1.5G illumination (100 mW cm $^{-2}$). The pristine BiFeO $_3$ electrode prepared by our synthesis is n-type 17 and therefore its J–V plot is not included in Fig. 4a. Bi-deficient

BiFeO $_3$ shows a well-defined cathodic photocurrent when light is on, indicating that the V_{Bi} generates acceptor levels increasing the hole concentration and making holes the majority carriers. Upon Na-doping, the cathodic photocurrent is further enhanced. For instance, at 0.6 V, Na-doped BiFeO $_3$ generates around $-200~\mu\text{A}~\text{cm}^{-2}$ whereas Bi-deficient BiFeO $_3$ generates only about $-50~\mu\text{A}~\text{cm}^{-2}$.

As Na-doped BiFeO₃ showed enhanced photon absorption relative to Bi-deficient BiFeO₃, a higher photocurrent generation was expected, but the observed enhancement is more than what can be explained by enhanced photon absorption. If we account for the increase in light absorption at each wavelength upon Na doping as shown in Fig. 2d and consider how many photons are available at each wavelength under 1 sun illumination, the photocurrent of the Na-doped sample should increase by 1.2fold compared to the Bi-deficient sample (details in the Experimental section). However, the observed enhancement in photocurrent is almost 3-fold at 0.6 V vs. RHE, meaning that Na doping also enhances electron-hole separation. This postulation is well supported when the APCE of the two samples are compared (Fig. 4b). The APCE result shows what fraction of the absorbed photons generates holes that are separated from photo-generated electron-hole pairs and collected as the photocurrent. As APCE inherently compensates for the difference in photon absorption between the two samples, the

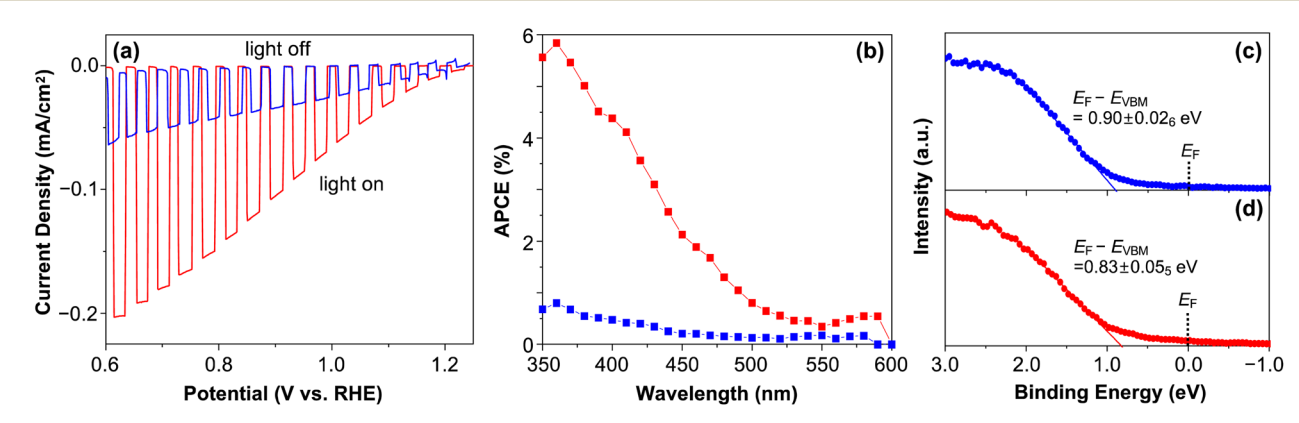


Fig. 4 (a) J-V plots of Bi-deficient (blue) and Na-doped (red) BiFeO₃ photoelectrodes for O₂ reduction in 0.1 M KOH under chopped AM 1.5G illumination (100 mW cm⁻²). (b) IPCE of Bi-deficient (blue) and Na-doped (red) BiFeO₃ at 0.6 V vs. RHE measured in O₂ purged 0.1 M KOH. Valence band (E_F-E_{VBM}) spectra of (c) Bi-deficient and (d) Na-doped BiFeO₃ photoelectrodes.

considerably higher APCE of Na-doped BiFeO3 directly shows the effect of Na-doping enhancing electron-hole separation. This result suggests that NaBi is a better acceptor than VBi and generates more free holes, which improves the hole conductivity and electron-hole separation. Another notable feature in the APCE results is that the photocurrent onset for the Nadoped sample occurs at a longer wavelength (610 nm, 2.03 eV) than that of the Bi-deficient sample (600 nm, 2.06 eV), confirming that the decreased bandgap caused by Na doping does allow lower-energy photons to be used for photocurrent generation.

If the Na-doped sample indeed has a higher hole concentration, its work function should be closer to the VBM than that of the Bi-deficient sample. This was probed by XPS analysis measuring the energy difference between the Fermi level and the valence band maximum (E_F - E_{VBM}) (Fig. 4c and d). The valence band spectra show that E_F - E_{VBM} of Bi-deficient BiFeO₃ is 0.9 eV while E_F - E_{VBM} of Na-doped BiFeO₃ is 0.83 eV. The fact that E_F of Na-doped BiFeO₃ is closer to the E_{VBM} than that of Bi-deficient BiFeO₃ by 70 meV confirms that the hole concentration in Nadoped BiFeO₃ is indeed higher than that of Bi-deficient BiFeO₃.

Ideally, a Bi³⁺ vacancy with a charge of 3- can be fully ionized to generate three holes while a Na+ dopant at the Bi3+ site with a charge of 2- can be fully ionized to generate two holes. Thus, a Bi vacancy has the capacity to achieve a higher hole concentration. However, this prediction simply based on the highest achievable charge state of each defect is applicable only when the formation energies for V_{Bi} and Na_{Bi} are comparable and both defects are shallow acceptors for all charge transfer levels. The fact that the Na-doped sample shows enhanced p-type behavior relative to the Bi-deficient sample indicates that their defect formation energies and/or ionization energies are different. Thus, we turned to computational studies to obtain an atomic level understanding of the differences between V_{Bi} and Na_{Bi} as p-type defects in BiFeO₃.

Defect formation energy and charge transition levels

We first examined the thermodynamic stability of the two defects, VBi and NaBi, through their defect formation and ionization energies. The formation energies and charge transition levels for V_{Bi} and Na_{Bi} are shown in Fig. 5. The oxygen chemical potential was computed for 1 atm at 873.15 K, to match experimental annealing conditions.33 More calculation details can be found in computational method section.

The charge transition level of an electron acceptor from one charge state to a more negative charge state referenced to the E_{VBM} defines the ionization energy of the p-type defect. For V_{Bi} that can have a charge of up to 3- by accepting three electrons, four charge states (0, -1, -2, -3) are possible. However, we only observed two transition levels in the bandgap, (0/-1) and (-1/-1)-2), which are equivalent to the first (0.43 eV) and second (1.14 eV) ionization energies of the V_{Bi} defect. For Na_{Bi} that can have up to a 2- charge, three charge states (0, -1, -2) are possible. Again, only two transition levels, (0/-1) and (-1/-2), are observed in the bandgap. The first and second ionization energies for Na_{Bi} are 0.10 eV and 0.16 eV, respectively.

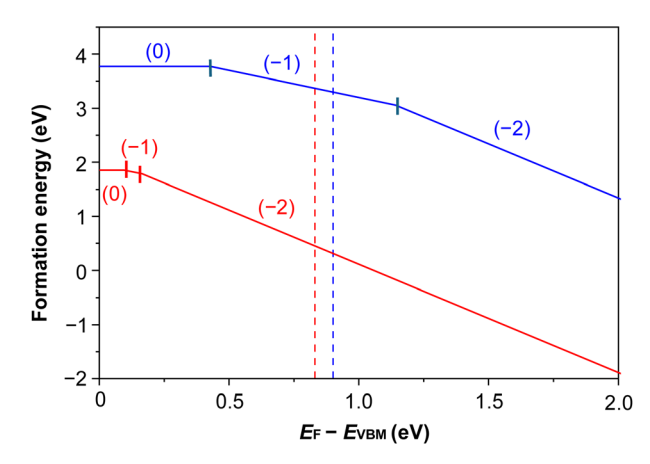


Fig. 5 Defect formation energy and charge transition levels of V_{Bi} (blue) and Na_{Bi} (red). The stable charge states as a function of E_{E} for each defect are denoted in the parenthesis. The dashed lines represent the experimentally determined $E_F - E_{VBM}$ of Bi-deficient BiFeO₃ (blue) and Na-doped BiFeO₃ (red).

Our experimental results obtained from XPS are found to be useful in assessing the stable charge state of V_{Bi} and Na_{Bi}. Fig. 4c and d show that E_F – E_{VBM} of Na-doped BiFeO₃ is 0.83 eV and that of Bi-deficient BiFeO₃ is 0.90 eV, which are marked as dashed lines in Fig. 5, suggesting that the stable charge states will be −1 for V_{Bi} and −2 for Na_{Bi} in these samples, meaning Na_{Bi} can create more free holes.

Another important consideration to assess the effect of dopants is their formation energy. Our results show that the formation energy of V_{Bi} is nearly 2 eV higher than that of Na_{Bi} in the p-type region (i.e., E_F - E_{VBM} < 1 eV). We note that these calculated values are obtained from a model having a perfect crystal structure and therefore the actual formation energies of Na_{Bi} and V_{Bi} in the real BiFeO₃ sample which has a polycrystalline/nanocrystalline nature with atoms in non-ideal coordination environments can be much lower. However, the qualitative trend that NaBi is much easier to form than VBi will be true for any case.

The combination of the computational and experimental results suggests that NaBi forms much more easily and is a shallower acceptor than V_{Bi}. As a result, Na-doped sample has a higher acceptor concentration and also more effectively increases the hole concentration, which results in a higher hole conductivity and higher electron-hole separation, generating higher cathodic photocurrent under illumination.

Hole polaron formation in Na-doped BiFeO₃

Next, we investigated the electronic structure of Na-doped BiFeO₃. The electronic band structure and projected density of states (PDOS) of pristine and Na-doped BiFeO₃ are compared in Fig. 6. The results show that Na doping generates isolated hole-polaron states about 0.3 eV above the E_{VBM} . The two holepolarons generated from Na doping appear to be localized around the O, Bi, and Fe atoms neighboring to the Na dopant (with no distribution on Na), as shown in Fig. 7. We note that the hole-polarons are much more delocalized compared to the

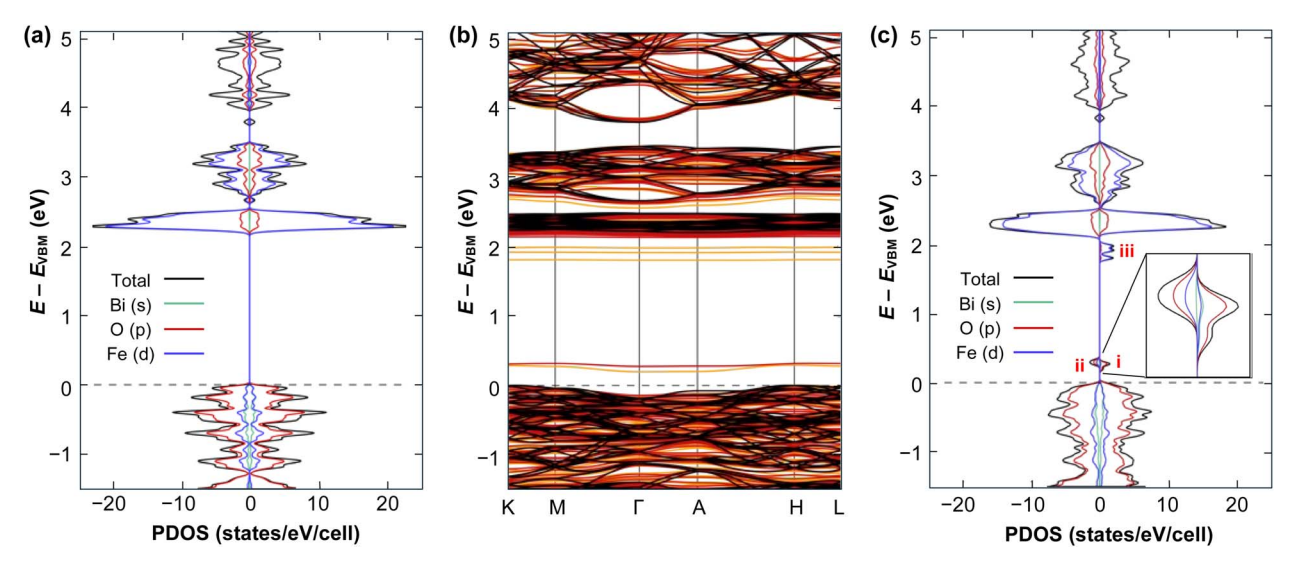


Fig. 6 PDOS for (a) pristine BiFeO₃ and (c) Na-doped BiFeO₃ with a single Na substitution of Bi in a 120-atom supercell (spin up states in positive values and spin down states in negative values). (b) Band structure of pristine BiFeO₃ (black) and spin resolved band structure of Na-doped BiFeO₃ (spin up in orange and spin down in red).

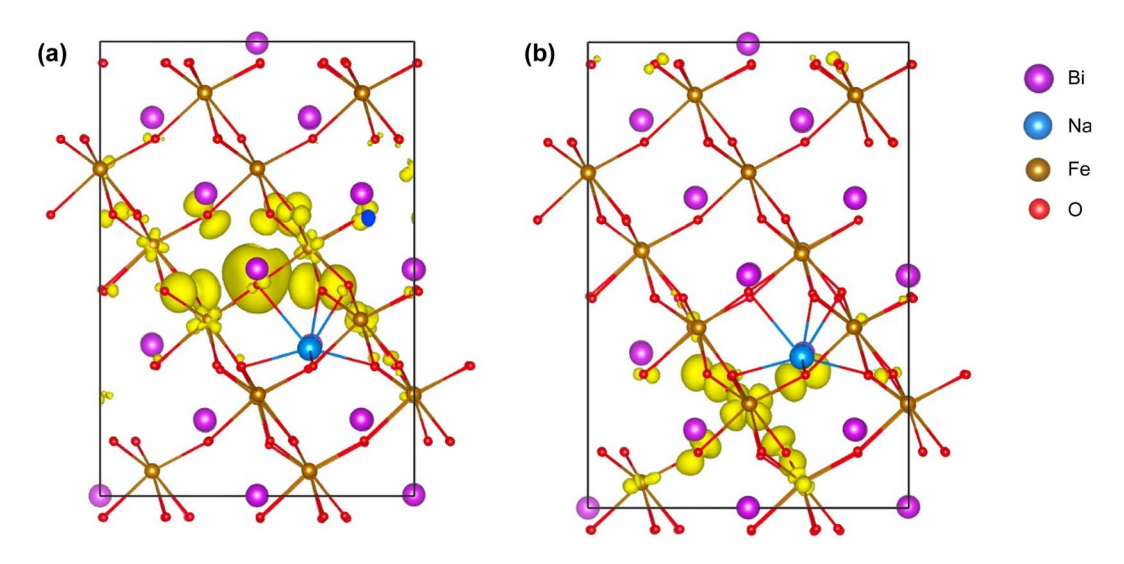


Fig. 7 Norm-squared wavefunctions of the two hole-polarons (yellow cloud) of Na-doped BiFeO₃ at 0.3 eV above the E_{VBM} with (a) spin up and (b) spin down configurations. The wave functions are shown as an isosurface in the Na-doped BiFeO₃ lattice and the isosurface value is 1% of the maximum amplitude of the wave function.

electron-polarons in BiFeO₃, which are highly localized on Fe atoms. 17 Between the two hole-polarons (i.e., spin up and spin down), the hole-polaron that is localized on Bi and O (spin up) has slightly lower energy (indicated by i in Fig. 6c). Specifically, it exhibits mostly Bi 6s character with some spread to oxygen 2p orbitals (Fig. 7a). The second hole-polaron with slightly higher energy (spin down, indicated by ii in Fig. 6c) localizes on one Fe and neighboring O atoms. In BiFeO₃, the Fe³⁺ has O_h crystal field splitting with 3d⁵ high-spin electron configuration.³⁸ Thus, a hole should firstly form at an Fe $e_{\rm g}$ state since they are higher in energy than the $t_{\rm 2g}$ states. Indeed, we observe $e_{\rm g}$ character for the hole density around Fe (Fig. 7b) and this localization of a hole on Fe increases the valency of Fe from 3+ to 4+. The

substitutional replacement of Bi by Na also generates perturbed conduction states. This perturbation can be seen as the localized states near the conduction band in Fig. 6c (indicated as iii). The three localized states near the CBM all have t_{2g} character of Fe as shown in Fig. S3.† The calculation results obtained with PBE + U shown in Fig. 7 and S3† were compared with the results obtained by calculations using hybrid functional HSE06.30 This comparison confirmed the reliability of the PBE + U (Fig. S4 and S5†).

Simulated absorption

In order to investigate whether the additional localized states appeared above the VBM and below the CBM can affect the

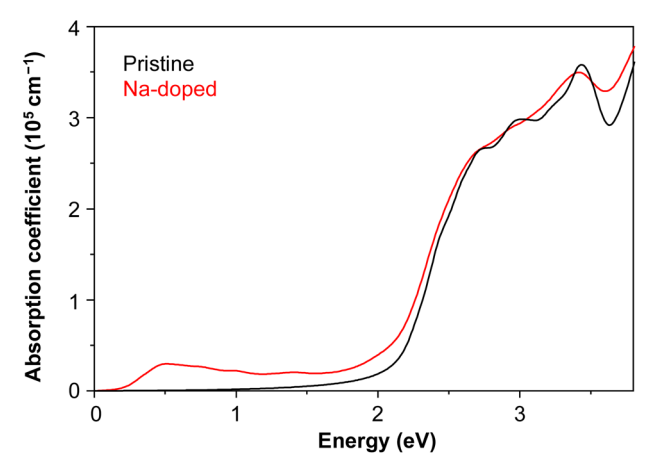


Fig. 8 Absorption coefficients for pristine BiFeO₃ (black) and Nadoped BiFeO₃ (red).

optical properties of BiFeO3, we calculated the absorption spectra of pristine and Na-doped BiFeO₃ (Fig. 8). Because of the presence of optical anisotropy in the system, we averaged optical responses from light that was polarized along the a, b, and c crystal axes. Excitonic effects were not included in this calculation because in most transition metal oxides, the exciton binding energy is small (\sim 0.1 eV) and its change by doping is negligible.39-41

When the Na dopant was introduced, two major changes appeared due to the formation of in-gap states: the perturbed conduction band states near the CBM and the hole states near the VBM, as discussed above. The first change results in the decrease in the bandgap energy by allowing electron transitions from the filled states in the valence band to the empty perturbed conduction band states (iii in Fig. 6c). This computational result explains the atomic origin of the experimentally observed redshift of the bandgap of Na-doped BiFeO3 compared to pristine BiFeO₃ (Fig. 2d). The second change leads to the enhanced background absorption below the bandgap energy by allowing transitions from the filled states in the valence band to the empty hole states above the VBM (i and ii in Fig. 6c). The onset of the background absorption at around 0.3 eV matches the

energy difference between the VBM and the hole states. In the experimental result where the absorbance was obtained above 1.8 eV (Fig. 2d), an enhancement in background absorption caused by Na doping was not noticeable.

Photoelectrochemical H₂O₂ production

We next explored the use of a Na-doped BiFeO₃ photocathode for the photoelectrochemical reduction of O₂ to H₂O₂. The conventional anthraquinone-based H2O2 synthesis requires centralized H₂O₂ production due to its complex processes.²³⁻²⁵ Electrochemical O₂ reduction to H₂O₂, which is much simpler and environmentally benign, has the potential to enable on-site H₂O₂ production, eliminating transportation and storage issues of H₂O₂.²³⁻²⁵ Electrochemical O₂ reduction at the cathode is typically paired with water oxidation at the anode. As the anode potential for water oxidation ($E^{0} = 1.229 \text{ V } \nu s. \text{ NHE}$)⁴² is more positive than the cathode potential for O_2 reduction (E^0 0.695 V vs. NHE), 42 an electrical energy input (E_{cell} in Fig. 9a) is needed to make the potential of the electrons obtained from water oxidation sufficiently negative for O2 reduction. However, if O2 reduction is performed photoelectrochemically using a photocathode (i.e., p-type BiFeO₃) with solar energy, photoexcited electrons in the CB are used for O2 reduction to H2O2. The electrons obtained from water oxidation at the anode are used only to fill the holes in the VB of BiFeO₃. Thus, the energy input required to operate the BiFeO₃-based photoelectrochemical cell for H_2O_2 production (E_{cell} in Fig. 9b) can be significantly reduced compared to the case of the electrochemical cell.

O₂ can be reduced to H₂O by 4-electron reduction as well as to H₂O₂ by 2-electron reduction. When O₂ was photoelectrochemically reduced by BiFeO₃ photocathodes in 0.1 M KOH solution (Fig. 4a), a negligible amount of H_2O_2 was produced, indicating that the bare BiFeO3 surface has no catalytic ability for 2-electron reduction of O2. Thus, in order to utilize photogenerated electrons for O2 reduction to H2O2, a catalyst that can promote 2-electron reduction of O2 needs to be placed on the BiFeO₃ surface. Previous studies have demonstrated that Ag metal catalysts can promote 2-electron O2 reduction in acidic media.43 We also recognized that Ag can be

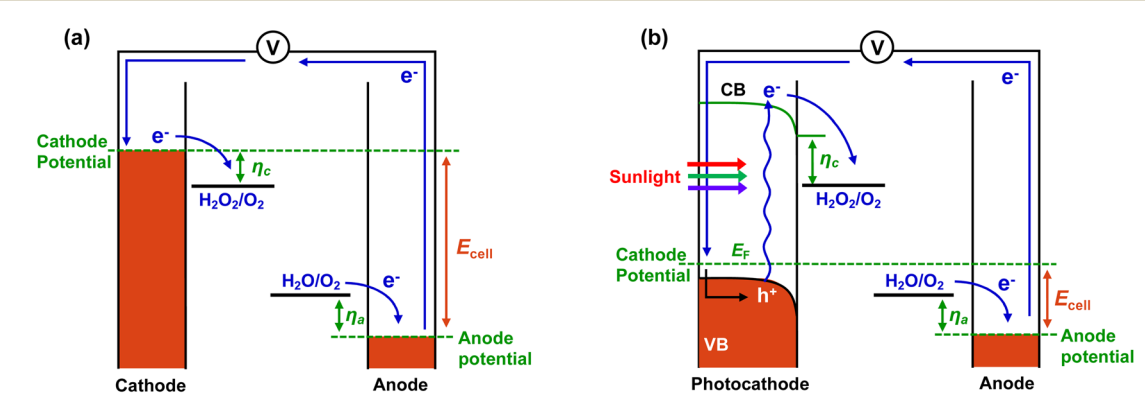


Fig. 9 Comparison of (a) electrochemical and (b) photoelectrochemical O₂ reduction paired with water oxidation. In (b), a photocathode is used to generate electron-hole pairs using absorbed photons

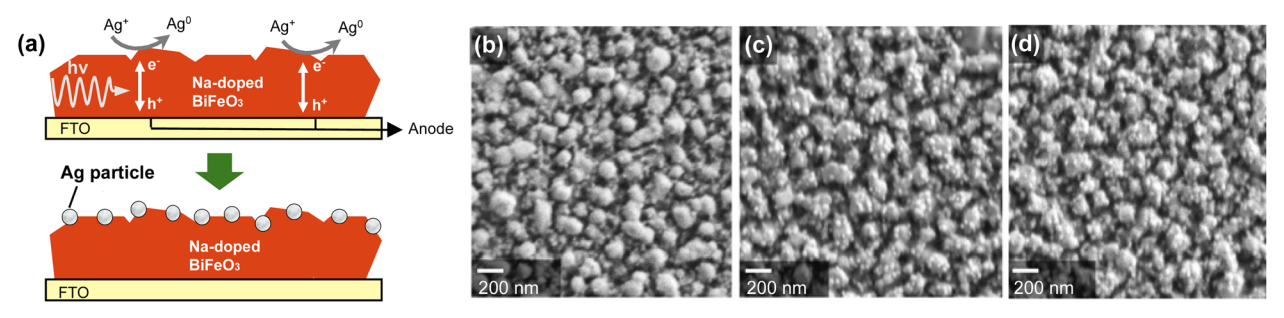


Fig. 10 (a) Schematic illustration of the photoelectrochemical deposition of Ag particles on Na-doped BiFeO₃ photocathodes. SEM images of (b) bare Na-doped BiFeO₃ (c) as-prepared Ag-deposited Na-doped BiFeO₃ where Ag catalysts appear as bright nanoparticles, and (d) Ag-deposited Na-doped BiFeO₃ after an 1 h-electrolysis.

photoelectrochemically deposited on BiFeO3 using photoexcited electrons in BiFeO3 under solar illumination because the reduction potential of Ag⁺ to Ag ($E^{o} = 0.7989 \text{ V } \nu s. \text{ NHE}$)⁴² is located below the CBM of BiFeO3. If Ag particles are photoelectrochemically deposited using photoexcited electrons in BiFeO₃, they will be automatically deposited where photoexcited electrons are readily available (Fig. 10a). This can help the resulting photoelectrochemically deposited Ag catalyst mostefficiently utilize photogenerated electrons in BiFeO₃ for O₂ reduction. The SEM images of Na-doped BiFeO3 before and after photo-electrodeposition of Ag are shown in Fig. 10b and c; Ag appears as bright nanoparticles evenly distributed on BiFeO₃ in Fig. 10c.

We tested Na-doped BiFeO3 with and without Ag for solar H₂O₂ production in O₂-saturated 0.1 M phosphate solution (pH 7) (Fig. 11a). A neutral electrolyte was used because the Ag catalyst is not active for 2-electron O2 reduction in alkaline media while BiFeO₃ is not stable in acidic media; thus, a neutral medium offers a reasonable condition to promote H₂O₂ production on a stable BiFeO₃ photocathode. Na-doped BiFeO₃ without Ag shows negligible photocurrent, indicating that the bare BiFeO₃ surface does not have good O₂ reduction kinetics (both for 2-electron and 4-electron reduction) in neutral media. However, the presence of Ag on Na-doped BiFeO3 greatly

enhanced photocurrent, suggesting that O2 reduction is indeed promoted by the Ag catalyst with the photocurrent onset being as positive as 1.28 V. This onset potential is more positive than E^{o} for O_2 reduction to H_2O_2 (0.695 V vs. RHE) by 0.585 V, showing the advantage of using photoexcited electrons in BiFeO₃ for O₂ reduction. When we obtained a J-V plot in the dark with the Ag catalyst deposited on FTO in the same solution, the onset of O₂ reduction appeared at 0.50 V vs. RHE, which is more negative than Eo for O2 reduction to H2O2 due to the requirement of an overpotential shown in Fig. 9a. If we define the photovoltage gain achieved by BiFeO3 for H2O2 production as the onset potential difference between the Ag catalyst on FTO in the dark and Ag catalyst deposited on Na-doped BiFeO3 under illumination, it is as high as 0.78 V (Fig. 11a, black arrow).

To quantitatively analyze H2O2 production, we performed a constant potential photoreduction of O2 at 0.8 V vs. RHE for an hour with continuous O2 purging. A stable photocurrent was obtained during the measurement (Fig. 11b), indicating the photostability of the electrodes under the operating condition. The SEM image taken after the photoelectrochemical O2 reduction reaction also confirmed no noticeable change in the morphology of either the Ag catalyst or the BiFeO3 photocathode (Fig. 10d). The amount of H2O2 was quantified by using iodometry (Fig. 11c), and the FE was calculated to be 40.1%. We

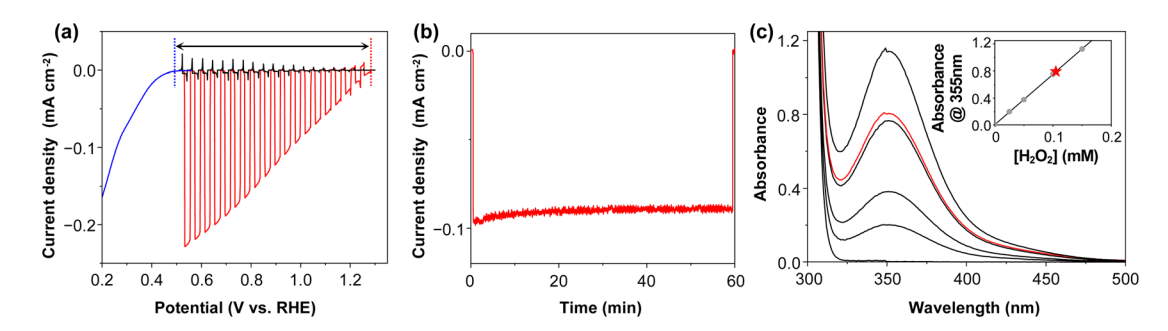


Fig. 11 (a) J-V plots of bare (black) and Ag-deposited (red) Na-doped BiFeO₃ electrodes in O₂ saturated 0.1 M phosphate buffer solution (pH 7) under chopped AM 1.5G illumination (100 mW cm^{-2}). The J-V plot obtained with the same amount of Ag-deposited FTO in the dark is shown for a comparison (blue). The photovoltage gain for H_2O_2 production by the use of Na-doped BiFeO₃ as a photocathode under illumination is indicated by the black arrow. The onset potential was chosen to be the potential where the current density reaches $1 \mu A$ cm⁻² (b) J-t plot of Agdeposited Na-doped BiFeO₃ at 0.8 V (vs. RHE) in the same solution under AM 1.5G illumination (100 mW cm⁻²). (c) UV-vis spectra for H_2O_2 quantification. Inset shows the calibration curve constructed based on the absorbance at 355 nm. The concentrations of the standards solutions were 0, 25, 50, 100, and 150 μM (black lines). The spectrum acquired with the solution from catholyte after the electrolysis is shown in red.

note that while 2-electron O2 reduction on BiFeO3 under illumination has been demonstrated previously, 18,44 we believe that our results are the first to show a photovoltage gain for photoelectrochemical H2O2 production occurring at the potential more positive than the thermodynamic reduction potential of 2electron O2 reduction, which is essential to demonstrate the true advantage of using a photocathode for solar H₂O₂ production.

Conclusions

In summary, we performed combined experimental and theoretical investigations to compare the effect of V_{Bi} and Na_{Bi} defects on the production of p-type BiFeO₃ photoelectrodes. The experimental results showed that the Na-doped sample achieved enhanced photon absorption and photocurrent generation compared to the Bi-deficient sample. The IPCE results revealed that the difference in photocurrent between these two samples is greater than that expected based on the difference in photon absorption, suggesting Na doping enhances both the generation and separation of electron-hole pairs. The valence band spectra showed that the Na-doped sample has a Fermi level closer to the VBM than the Bi-deficient one, meaning NaBi increases the hole concentration more effectively than V_{Bi} , resulting in a better hole transport in BiFeO3 and a higher electron-hole separation. The computational results revealed that the formation energy of NaBi is smaller than that of VBi. Also, the ionization energies of Na_{Bi} are lower than those of V_{Bi} . These results explained why the Na-doped sample showed enhanced p-type behavior compared to the Bi-deficient sample. The computational results also showed that Na doping results in the formation hole states above the VBM and perturbed conduction band states below the CBM and the latter is responsible for a decrease in the bandgap. When the Na-doped BiFeO₃ was coupled with a Ag catalyst for use in solar O₂ reduction, H2O2 was produced with a FE as high as 40.1% in a pH 7 solution at 0.8 V vs. RHE. By utilizing photoexcited electrons in the CB of BiFeO₃ for O₂ reduction, H₂O₂ could be produced at a potential more positive than the thermodynamic reduction potential of O₂ to H₂O₂, demonstrating the advantage of solar H₂O₂ production using a photocathode.

Data availability

Data for this article are available at https://github.com/Ping-Group-UCSC/2024-BiFeO3-Data/tree/main.

Conflicts of interest

The authors declare no competing interests.

Acknowledgements

This work was supported by the Division of Chemical Sciences, Geosciences, and Biosciences, Office of Basic Energy Sciences of the U.S. Department of Energy through Grant DE-SC0024211. Ping acknowledges the support from the National Science

Foundation under grant no. CHE-2203633. This work used the computational resources of the Scientific Data and Computing center, a component of the Computational Science Initiative, at Brookhaven National Laboratory under Contract No. DEthe National Energy Research Computing Center (NERSC), a U.S. Department of Energy Office of Science User Facility operated under Contract No. DE-AC02-05CH11231. This work also used the computational resources on Bridges at PSC through allocation DMR160106 from the Cyberinfrastructure Coordination Services & Support (ACCESS) program, which is supported by National Science Foundation grants #2138259, #2138286, #2138307, #2137603, and #2138296.

References

- 1 S. R. Burns, O. Paull, J. Juraszek, V. Nagarajan and D. Sando, Adv. Mater., 2020, 32, 2003711.
- 2 T. Choi, S. Lee, J. Choi, V. Kiryukhin and S.-W. Cheong, Science, 2009, 324, 63-67.
- 3 H. T. Yi, T. Choi, S. G. Choi, Y. S. Oh and S. W. Cheong, Adv. Mater., 2011, 23, 3403-3407.
- 4 M. B. Holcomb, Q. He, P. Maksymovych, N. Balke, S. V. Kalinin, A. P. Baddorf and S. R. Basu, Nat. Mater., 2009, 8, 485-493.
- 5 H. Shen, X. Zhou, W. Dong, X. Su, L. Fang, X. Wu and M. Shen, Appl. Phys. Lett., 2017, 111, 123901.
- 6 P. Yilmaz, D. Yeo, H. Chang, L. Loh and S. Dunn, Nanotechnology, 2016, 27, 345402.
- 7 Q. Liu, Y. Zhou, L. You, J. Wang, M. Shen and L. Fang, Appl. Phys. Lett., 2016, 108, 022902.
- 8 J. Song, T. L. Kim, J. Lee, S. Y. Cho, J. Cha, S. Y. Jeong, H. An, W. S. Kim, Y. Jung, J. Park, G. Y. Jung, D. Kim, J. Y. Jo, S. D. Bu, H. W. Jang and S. Lee, *Nano Res.*, 2018, **11**, 642–655.
- 9 S. J. A. Moniz, C. S. Blackman, P. Southern, P. M. Weaver, J. Tang and C. J. Carmalt, Nanoscale, 2015, 7, 16343-16353.
- 10 Y.-L. Huang, W. S. Chang, C. N. Van, H.-J. Liu, K.-A. Tsai, J.-W. Chen, H.-H. Kuo, W.-Y. Tzeng, Y.-C. Chen and C.-L. Wu, Nanoscale, 2016, 8, 15795-15801.
- 11 S. Das, P. Fourmont, D. Benetti, S. G. Cloutier, R. Nechache, Z. M. Wang and F. Rosei, J. Chem. Phys., 2020, 153, 084705.
- 12 W. Ji, K. Yao, Y. Lim, Y. C. Liang and A. Suwardi, Appl. Phys. Lett., 2013, 103, 062901.
- 13 D. K. Lee, D. Lee, M. A. Lumley and K. S. Choi, Chem. Soc. Rev., 2019, 48, 2126-2157.
- 14 T. R. Paudel, S. S. Jaswal and E. Y. Tsymbal, Phys. Rev. B: Condens. Matter Mater. Phys., 2012, 85, 1-8.
- 15 S. Farokhipoor and B. Noheda, J. Appl. Phys., 2012, 112,
- 16 T. Rojac, A. Bencan, G. Drazic, N. Sakamoto, H. Ursic, B. Jancar, G. Tavcar, M. Makarovic, J. Walker and B. Malic, Nat. Mater., 2017, 16, 322-327.
- 17 A. Radmilovic, T. J. Smart, Y. Ping and K. S. Choi, Chem. Mater., 2020, 32, 3262-3270.
- 18 B. Tan, A. M. Reyes, E. Menéndez-Proupin, S. E. Reyes-Lillo, Y. Li and Z. Zhang, Full-Space Potential Gradient Driven

- Charge Migration inside BiFeO₃ Photocathode, *ACS Energy Lett.*, 2022, 7, 3492–3499.
- 19 N. P. Prasad, M. Rohnke, M. A. Verheijen, J. M. Sturm, J. P. Hofmann, E. J. M. Hensen and A. Bieberle-Hütter, *ACS Appl. Energy Mater.*, 2023, **6**, 12237–12248.
- 20 S. Yang, A. Verdaguer-Casadevall, L. Arnarson, L. Silvioli, V. Čolić, R. Frydendal, J. Rossmeisl, I. Chorkendorff and I. E. L. Stephens, ACS Catal., 2018, 8, 4064–4081.
- 21 E. Jung, H. Shin, W. Hooch Antink, Y. E. Sung and T. Hyeon, *ACS Energy Lett.*, 2020, **5**, 1881–1892.
- 22 M. Ko, J. S. Lim, J. W. Jang and S. H. Joo, ACS ES&T Eng., 2023, 3, 910-922.
- 23 J. Rodríguez-Carvajal, *An Introduction to the Program FullProf* 2000, Laboratoire Leon Brillouin (CEA-CNRS), France, 2001.
- 24 I. Sosnowska, W. Schäfer, W. A. Kockelmann and I. O. Troyanchuk, *Mater. Sci. Forum*, 2001, 378, 616–620.
- 25 ASTM Standard G173-03 (Reapproved 2008), Standard Tables for Reference Solar Spectral Irradiances: Direct Normal and Hemispherical on 37° Tilted Surface, ASTM International, West Conshohocken, Pennsylvania, 2003.
- 26 P. Giannozzi, S. Baroni, N. Bonini, M. Calandra, R. Car, C. Cavazzoni, D. Ceresoli, G. L. Chiarotti, M. Cococcioni, I. Dabo, A. Dal Corso, S. de Gironcoli, S. Fabris, G. Fratesi, R. Gebauer, U. Gerstmann, C. Gougoussis, A. Kokalj, M. Lazzeri, L. Martin-Samos, N. Marzari, F. Mauri, R. Mazzarello, S. Paolini, A. Pasquarello, L. Paulatto, C. Sbraccia, S. Scandolo, G. Sclauzero, A. P. Seitsonen, A. Smogunov, P. Umari and R. M. Wentzcovitch, J. Phys.: Condens. Matter, 2009, 21, 395502.
- 27 K. F. Garrity, J. W. Bennett, K. M. Rabe and D. Vanderbilt, *Comput. Mater. Sci.*, 2014, **81**, 446–452.
- 28 R. Sundararaman and Y. Ping, J. Chem. Phys., 2017, 146, 104109.

- 29 R. Sundararaman, K. Letchworth-Weaver, K. A. Schwarz, D. Gunceler, Y. Ozhabes and T. A. Arias, *SoftwareX*, 2017, 6, 278–284.
- 30 A. V. Krukau, O. A. Vydrov, A. F. Izmaylov and G. E. Scuseria, J. Chem. Phys., 2006, 125, 224106.
- 31 G. Kresse and J. Furthmüller, *Phys. Rev. B: Condens. Matter Mater. Phys.*, 1996, **54**, 11169–11186.
- 32 A. Marini, C. Hogan, M. Grüning and D. Varsano, *Comput. Phys. Commun.*, 2009, **180**, 1392–1403.
- 33 T. J. Smart, M. Chen, A. C. Grieder, V. Urena Baltazar, F. Bridges, Y. Li and Y. Ping, *J. Appl. Phys.*, 2021, 130, 245705.
- 34 R. D. Shannon, Acta Crystallogr., 1976, 32, 751-767.
- 35 G. P. Wheeler, V. U. Baltazar, T. J. Smart, A. Radmilovic, Y. Ping and K. S. Choi, *Chem. Mater.*, 2019, 31, 5890–5899.
- 36 D. Kang, J. C. Hill, Y. Park and K. S. Choi, *Chem. Mater.*, 2016, 28, 4331–4340.
- 37 R. A. Afzal, K. Y. Park, S. H. Cho, N. I. Kim, S. R. Choi, J. H. Kim, H. T. Lim and J. Y. Park, RSC Adv., 2017, 7, 47643–47653.
- 38 P. Baettig, C. Ederer and N. A. Spaldin, *Phys. Rev. B: Condens. Matter Mater. Phys.*, 2005, 72, 214105.
- 39 T. Kim, Y. Ping, G. Galli and K. S. Choi, *Nat. Commun.*, 2015, 6, 8769.
- 40 Y. Ping, D. Rocca and G. Galli, *Phys. Rev. B: Condens. Matter Mater. Phys.*, 2013, **87**(16), 165203.
- 41 Y. Ping and G. Galli, *J. Phys. Chem. C*, 2014, **118**(12), 6019–6028.
- 42 A. J. Bard, L. R. Faulkner and H. S. White, *Electrochemical Methods: Fundamentals and Applications*, John Wiley & Sons, New Jersey, 2022.
- 43 B. B. Blizanac, P. N. Ross and N. M. Markovic, *Electrochim. Acta*, 2007, 52, 2264–2271.
- 44 Z. Zhang, B. Tan, W. Ma, B. Liu, M. Sun, J. K. Cooper and W. Han, *Mater. Horiz.*, 2022, **9**, 1999.